Online Tissue Discrimination for Transcutaneous Needle Guidance Applications Using Broadband Impedance Spectroscopy

Dennis Trebbels*, Felix Fellhauer, Michael Jugl, Gerd Haimerl, Mart Min, and Roland Zengerle

***Abstract*—This paper reports on a novel system architecture for measuring impedance spectra of a biological tissue close to the tip of a hollow needle. The measurement is performed online using fast broadband chirp signals. The time domain measurement raw data are transformed into the transfer function of the tissue in frequency domain. Correlation technique is used to analyze the characteristic shape of the derived tissue transfer function with respect to known "library functions" for different types of tissue derived in earlier experiments. Based on the resulting correlation coefficients the exact type of tissue is determined. A bipolar coaxial needle is constructed, simulated by finite element method and tested during various *in vitro* and *in vivo* experiments. The results show a good spatial resolution of approximately 1.0 mm for a needle with a diameter of 2.0 mm. The correlation coefficients for the three tested tissue types muscle, fat, and blood allow for a clear tissue classification. Best results have been obtained using the characteristic phase diagrams for each tissue. Correlated to the corresponding library transfer function the coefficients are in the range of $+0.96$ to $+0.99$ for the matching tissue. In return, the resulting coefficients for correlation with nonmatching tissues are in the range of -0.93 to $+0.81$.**

***Index Terms*—Broadband impedance spectroscopy, cannula guidance, chirp-signals, needle guidance, tissue classification.**

I. Introduction

NEEDLE guidance during transcutaneous surgical interventions is a common challenge in many medical applications such as fine needle biopsies [1], regional anaesthesia [2], drug delivery [2], catheter insertion [3], vessel puncture [4] and brachytherapy [5]. In all of the listed applications it is important to place the needle tip inside a well defined tissue type of the human body whereas often the exact 3-D orientation of the needle is of minor importance.

Today there are several approaches to accomplish the exact needle placement based on 2-D or 3-D imaging systems which allow for controlling the needle orientation and position and support the surgeon during the needle insertion procedure. Three well known systems are magnetic resonance imaging (MRI), computed tomography (CT) and X-Ray fluoroscopy [6]–[8]. All systems work very well and give good spatial resolution but are too expensive for widespread use. In addition CT and X-Ray fluoroscopy expose the patient to ionizing radiation. Furthermore, fluoroscopy provides only a limited contrast for soft-tissues, which is a crucial point for needle guidance. Alternative imaging systems are based on ultrasound (US) [9], [10]. There are several ultrasound systems available in the market, but major drawbacks are the limited penetration depth and the limited field of view. In addition, it is difficult to analyze the exact type of soft tissue close to the needle tip by using US. The use of force-feedback systems [11] in combination with imaging based systems or robots [12] can improve the needle steering process but the overall system again becomes quite complicated and expensive. In some actual research projects microsensors are integrated in the needle tip [13] but deal with the inherent lack of space given by the thin needle geometry and the low-cost requirements for disposable medical equipment.

A promising alternative approach for exact online tissue classification at the needle tip during the insertion process into the human body is broadband impedance measurement, often referred to as impedance spectroscopy (IS). This method is based on the continuous measurement of the characteristic impedance spectrum of a small volume of tissue around the needle tip. The measured spectrum is analyzed and the exact type of tissue can be determined. Kalvoy *et al*. already presented preliminary results of their configuration based on a monopolar needle electrode where the impedance is measured against a reference electrode [14], [15]. The results look promising but a drawback of the system is the need for the additional reference electrode, and due to the current density distribution the achievable spatial resolution is limited to a spherical volume having a diameter of approximately three to four times the needle diameter. We already proposed a coaxial needle design in combination with time domain reflectometry (TDR) measurement technique [16]. Drawback of this technique is the poor signal-to-noise ratio, which can be achieved for a broadband measurement.

Manuscript received March 8, 2011; revised June 9, 2011 and August 25, 2011; accepted October 3, 2011. Date of publication November 8, 2011; date of current version January 20, 2012. *Asterisk indicates corresponding author.*

*D. Trebbels, HSG-IMIT, Institut für Mikro- und Informationstechnik der Hahn-Schickard-Gesellschaft e.V., 78052 Villingen-Schwenningen, Germany (e-mail: dennis.trebbels@hsg-imit.de).

F. Fellhauer, HSG-IMIT, Institut für Mikro- und Informationstechnik der Hahn-Schickard-Gesellschaft e.V., 78052 Villingen-Schwenningen, Germany (e-mail: felix.fellhauer@hsg-imit.de).

M. Jugl and G. Haimerl are with the HFU, Hochschule Furtwangen University, 78054 Villingen-Schwenningen, Germany (e-mail: michael.jugl@hsg-imit.de; hai@hs-furtwangen.de).

M. Min is with the Tallinn University of Technology, Faculty of Information Technology, Department of Electronics, 19086 Tallinn, Estonia (e-mail: min@elin.ttu.ee).

R. Zengerle is with the Department of Microsystems Engineering, Laboratory for MEMS-Applications, University of Freiburg, 79110 Freiburg, Germany (e-mail: roland.zengerle@gmx.de).

Color versions of one or more of the figures in this paper are available online at http://ieeexplore.ieee.org.

Digital Object Identifier 10.1109/TBME.2011.2174990

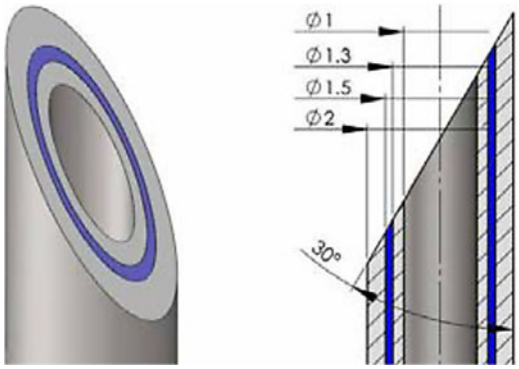

Fig. 1. Detailed view of the constructed coaxial hollow needle. The needle consists of two concentric stainless steel tubes which are electrically isolated by an inner layer of Teflon (PTFE). The given dimensions correspond to the prototype needle, which is used throughout the simulations and experiments.

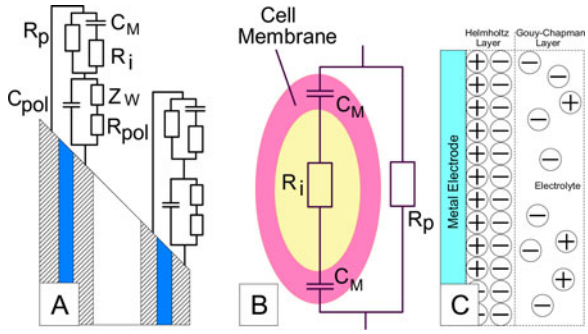

Fig. 2. (a) Equivalent electrical schematic of biological tissue located on the needle tip in series to a model for the electrode polarization. (b) The used cell model from which the equivalent schematic is derived. (c) The electrode polarization effect by a double layer structure.

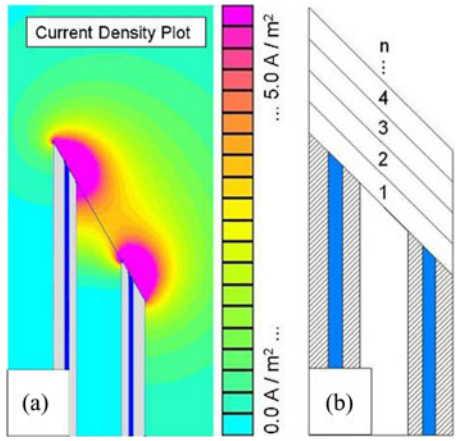

Fig. 3. (a) Current density plot of the needle tip in homogeneous resistive media. The highest current density and therefore the highest sensitivity are close to the needle tip. (b) The simulated needle tip and the volume virtually divided in front of the tip in thin slices with 0.1 mm thickness for further analysis of the losses and sensitivity. The results are shown in Fig. 4.

In this paper, we present a new measurement system for coaxial hollow needles where the impedance measurement method is based on short broadband chirp signals. The paper discusses the system concept, finite element method simulation results for the expected spatial resolution, chirp signal properties and processing, the developed laboratory measurement setup and experimental details for the conducted *in vitro* and *in vivo* experiments. The derived raw data are processed and analyzed by correlation techniques. The correlation results are presented and discussed particularly with regard to tissue classification. In addition, some further experiments are done in order to support the simulation results, investigating the impact of the speed of the needle during insertion process and evaluating the robustness of the classification method with regard to mechanical tolerances and imperfections of the needle.

II. System Concept and Model

Goal of the developed system is to continuously analyze and classify the exact type of tissue close to the needle tip during the insertion process of the needle into the human body. In order to classify the tissue close to the needle tip we continuously measure the complex electrical impedance of the tissue close to the needle tip at various frequencies within the range of 5 kHz to 1 MHz. Within this frequency range the complex transfer function of the tissue is expected to be characteristic for each individual type of tissue [17]. The chosen range is a compromise between overall bandwidth, signal duration, and the resulting total amount of raw data, which must be processed in real time. A more detailed description of the signal properties is given in Section IV-C.

A coaxial hollow needle is constructed as illustrated in Fig. 1. The inner stainless steel tube serves as electrical conductor for the measurement signal whereas the outer stainless steel tube is at ground potential. The two tubes are electrically isolated against each other by a thin layer of Teflon (PTFE). Current can only flow from the inner conductor to the outer conductor at the needle tip while inserted into a conductive media (see also Fig. 3). When the needle is inserted into biological tissue, the tissue forms a frequency-dependent electrical load on the needle tip as illustrated in Fig. 2(a). The presented equivalent circuit model for the tissue is composed of R_p, R_i, and C_M. Fig. 3(b) illustrates a corresponding cell model, where R_i represents the resistive behavior of the intracellular volume, R_p represents the resistive behavior of the extracellular volume, and C_M represents the capacitive behavior of the cell membrane [18]. In series to the tissue model we place a second model, which describes the frequency depending behavior of electrode polarization effects (C_{pol}, R_{pol}, Z_W) [19]. Electrode polarization occurs whenever a galvanically coupled metal electrode is in direct contact with an aqueous electrolyte. The effect can be explained by a rigid double layer, which is caused by metal ions on the electrode surface and corresponding counter ions in the electrolyte. Often this layer is referred to as Helmholtz layer. In addition, there is a weaker diffusion layer caused by the electrostatic coulomb forces of the charged metal surface, often referred to as Gouy-Chapman layer [see Fig. 2(c)]. The equivalent circuit model for the two layers consists of a common layer capacitance C_{pol} and the two elements R_{pol} and Z_W [19]. R_{pol} represents the resistive behavior of the charge transfer within the Helmholtz layer and is almost frequency independent. Z_W represents the impedance

of the Gouy-Chapman layer and is frequency-dependent. Often this frequency dependency is modeled by a constant phase element. The resistive properties of the electrolyte bulk material are already represented by R_p of the tissue model, and therefore here not included in the double layer model.

For tissue classification,it would be ideal to measure the broadband impedance of the tissue only and eliminating the parasitic effects caused by the electrode polarization. However, this is practically impossible due to the 2-electrode interface formed by the needle tip. All measurement results will always be a combination of the tissue transfer function and the electrode polarization transfer function. Calibration and precision correction of the polarization effects is also practically not applicable because the polarization itself depends on characteristic tissue properties such as the conductivity of the bulk material as well as on measurement signal parameters such as the applied voltage level and the resulting current density. In addition, a calibration (e.g., in saline) for each hollow needle means a significant amount of work. In the ideal case, it would be possible to measure directly without the need for any calibration procedure.

Throughout the study presented here in this paper, we decided to go a straight way and simply measure the resulting overall electrode impedance as a function of frequency inside different types of tissue including all polarization effects. Multiple complex impedance curves are recorded for each type of tissue. An averaged curve for each individual tissue type is calculated out of the recorded data and serves as "library function." Tissue classification is done by comparing these "tissue library functions" online with continuously measured impedance curves. The comparison is made by correlation and the tissue classification is based on the resulting correlation coefficients. We accept that the measured impedance curves do not exactly represent the specific tissue impedance only. Our focus is on tissue classification between several types of tissue and not on precise tissue analysis of one specific single tissue. The results discussed later in the paper show that a pure classification can be achieved by this method, and there is no need for an additional calibration procedure using a reference electrolyte.

III. Simulation

A low frequency finite element simulation is done in order to evaluate the current density distribution and the resulting spatial sensitivity for a needle with the geometry shown in Fig. 1. The simulation is done at a frequency of 100 kHz using the software package "Ansys Multiphysics." The maximum mesh size is set to 30 μm, the boundaries of the simulated volume are at ground potential. The excitation signal amplitude is set to 1 V and the conductivity of the bulk material is set to 1 S/m. However, the absolute values of the resistive bulk material and the excitation signal amplitude are not relevant, since we calculate the "relative losses." This means we calculate the losses within a small tissue volume close to the needle tip and compare them to the total losses in the simulated system caused by the measurement signal. Any absolute material properties such as the specific conductivity cancel out. The resulting "relative losses" represent the sensitivity as a function of the needle tip geometry only. We do not simulate any frequency-dependent behavior of the tissue since this has no effect on the spatial sensitivity. The electrical losses are proportional to the square of the current density within a small volume of tissue. Fig. 3(a) shows a simulated current density pattern for the needle tip inserted into homogeneous resistive media.

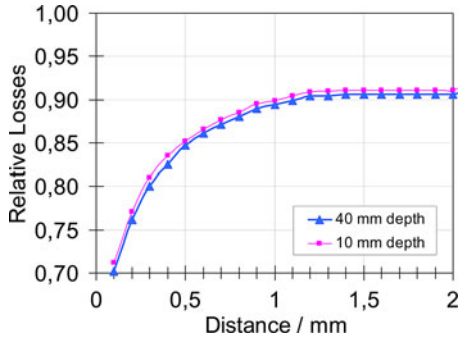

Fig. 4. FEM-Simulation results: Relative losses as a function of the volume in front of the needle tip. The volume is indicated by the distance to the needle tip according to the slices shown in Fig. 3.

As expected, the highest current density and, therefore, the highest sensitivity are found close to the needle tip, which serves as two-electrode-pair. For further detailed analysis of the sensitivity we virtually cut the volume in front of the needle tip into thin slices with a thickness of 0.1 mm each, as shown in Fig. 3(b). Fig. 4 presents the simulation result. The graph shows the accumulated relative losses inside a volume in front of the needle tip, as illustrated in Fig. 3(b). The graph shows that approximately 90% of the total losses are generated within a distance of only 1 mm to the needle tip. In addition, we investigated the effect of the needle insertion depth. The current density on the outer needle wall surface is very low but, in total, the needle has a large surface compared to the needle tip. Fig. 4 contains two graphs, one for 10 mm insertion depth and the other for 40 mm insertion depth. Both graphs are almost identical which means the sensitivity is almost independent of the insertion depth of the needle. The result looks reasonable since almost all losses ($\sim$90 %) are generated directly in front of the needle tip.

The simulation result leads to the assumption that the hollow coaxial needle design yields a very good spatial resolution of the measurement and is ideally suited for precision needle tip positioning. In addition to the simulation, we conducted an *in vitro* experiment. The obtained results support the simulation result very well and are described in detail within Sections VI and VII of this paper.

IV. Measurement Signals and Processing

A. Measurement Signals

As already mentioned in Section II, the measurement system must be capable of measuring the complex impedance spectrum of the tissue under investigation at the needle tip. Since needle insertion is a dynamic process, the measurement has to be done within a short period of time. In an ideal case the

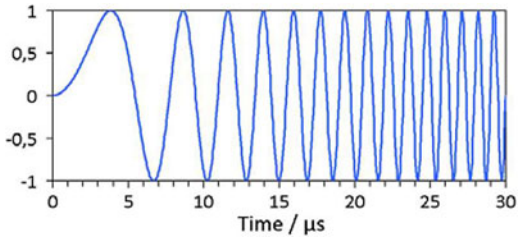

Fig. 5. Normalized linear chirp signal plot in time domain. The presented sample signal has a duration of 30 μs and its frequency ranges from 5 kHz to 1 MHz.

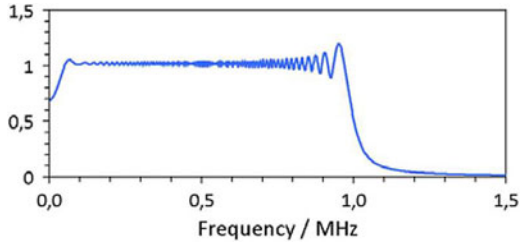

Fig. 6. Normalized amplitude plot of the power spectral density of the chirp signal presented in Fig. 5. The signal energy equally distributed within the bandwidth of the signal and therefore allowing broadband measurements with a stable signal to noise ratio over the whole frequency range.

measurement time window is so short that the complex tissue load on the needle tip remains stable for one complete measurement cycle. However, this requirement cannot be achieved by using conventional measurement techniques such as applying several frequencies within one slow sweep. Therefore, we use short broadband signals. One type of broadband signals is the so called chirp signal which has already been introduced as a promising signal for impedance measurement [20]. The sine wave based chirp signal has a general expression

$$C(t) = A\sin\theta\,(t) = A\sin\left\{\int \omega(t)dt + \theta_0\right\} \qquad (1)$$

with amplitude A, running phase θ(t), instantaneous angle frequency ω(t) and initial phase angle θ_0. A simple linear chirp has an instantaneous frequency $\omega(t) = d\theta(t)/dt$, which changes linearly during the excitation interval $T_{\rm exc}$ with constant acceleration $d\omega(t)/dt = d^2\theta(t)/dt^2 = k_{\rm ch}$. Expressing $\omega = 2\pi f$ and denoting f_0 as an initial, and $f_{\rm fin}$ as a final frequency, also taking $\theta_0 = 0$ and marking $T_{\rm ch}$ as duration of the chirp pulse, we obtain the following expression for the linear chirp excitation:

$$C1\,(t) = A\sin\left(2\pi\left(f_0\cdot t + (f_{\rm fin} - f_0)\cdot\frac{t^2}{2T_{\rm ch}}\right)\right). \qquad (2)$$

The excitation bandwidth $B_{\rm exc} = f_{\rm fin} - f_0$ remains the same when the excitation time $T_{\rm exc} = T_{\rm ch}$ changes. Only the chirping rate $k_{\rm ch} = (f_{\rm fin} - f_0)/T_{\rm ch}$ and signal energy $E = (A^2/2)T_{\rm ch}$ vary together with $T_{\rm ch}$.

A linear chirp signal calculated by (2) gives maximum flexibility in scaling the signal to the needs of the application. In this case amplitude, signal duration and covered bandwidth can be controlled independently. Figs. 5 and 6 show a linear chirp signal in time domain and frequency domain. One advantageous property of such a chirp signal is the flat spectrum in the frequency domain. The amplitude of all contained frequency bins remains stable over the entire frequency range (Fig. 6).

This property allows for measuring the impedance over the full bandwidth with stable signal-to-noise ratio and, therefore, leads to precision transfer functions of the measured complex needle tip impedance.

B. Signal Processing Concept

Goal of the measurement is to derive the complex transfer function of the load impedance caused by the tissue under investigation in the frequency domain. Therefore, the unknown tissue is stimulated by a broadband chirp voltage signal and the resulting response current is recorded. Both signals are synchronously sampled by a two-channel AD-converter and transformed into frequency domain (Fig. 7). The quotient of both signals is the complex transfer function.

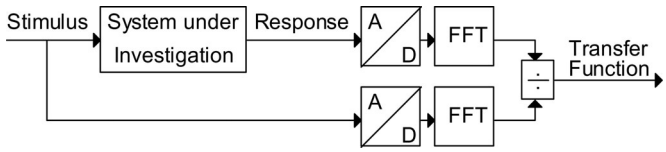

Fig. 7. Block schematic of the signal processing chain as implemented in the developed system. The system under investigation is the load impedance caused by the unknown tissue located at the needle tip. Stimulus and response signals are voltage and current signals, respectively. Both signals are sampled and converted into frequency domain for calculation of the transfer function.

C. Measurement Signal Properties

As already mentioned before, the chirp signal properties can independently be adjusted to the specific requirements of the application. In this case the bandwidth of interest is set to 5 kHz – 1.0 MHz, because here we expect a characteristic impedance spectrum for each biological tissue [17]. Furthermore, the covered frequency range is a compromise between the excitation signal bandwidth, excitation signal duration, and the resulting amount of sampled raw data, which must be processed online with a reasonable amount of computing effort. Key consideration is the required sampling rate of the two synchronous AD-converters shown in Fig. 7. According to the Shannon theorem, the minimum sampling rate must be at least twice the frequency of the highest frequency component in the signal. Therefore, the maximum frequency component $f_{\rm max}$ in the chirp signal dictates the minimum sampling frequency $f_{\rm sample\text{-}min}$ of both AD-converters which is $f_{\rm sample\text{-}min} = 2 * f_{\rm max}$. The resulting minimum total number of samples $N_{\rm min}$ required to capture one full chirp excitation signal can be calculated and expresses as $N_{\rm min} = T_{\rm chirp} * f_{\rm sample\text{-}min} = 2 * f_{\rm max} / f_{\rm min}$. This equation shows that the number of samples $N_{\rm min}$ is an exponential function and becomes quite large for signals with a broad bandwidth covering several decades. Therefore we choose a compromise and use a chirp signal with a duration of 200 μs. This results in a frequency resolution $\delta f = 1/T_{\rm chirp} = 1/200\,\mu{\rm s} = 5$ kHz and a minimum number of samples $N_{\rm min} = 400$. In addition we decide to use an oversampling rate of a factor 10, resulting in

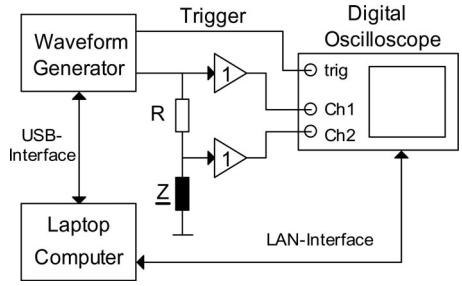

Fig. 8. Block schematic of the laboratory setup. The unknown impedance Z and the current measurement resistor are connected in series and the AWG excites the measurement signal. In addition, the AWG also generates an adjustable trigger signal for the oscilloscope that allows a customized sampling rate.

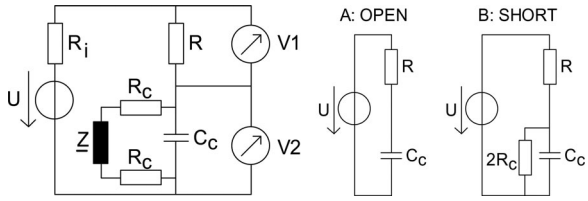

Fig. 9. Equivalent electrical schematic of the system including relevant parasitic components that cause measurement errors. R_i is the output resistance of the generator, R_c is the dc-resistance of the copper wires that connect the measurement setup with the needle and C_c is the cable capacitance of the used coaxial cable. (a) C_c can be estimated by an "open" calibration. (b) R_c can be estimated by a "short" calibration if C_c is known.

4000 samples. The next matching power of 2 is 4096 samples. The sampling frequency and thus the trigger frequency for the AD-converter is, therefore, adjusted to 20.48 MHz for capturing a chirp with $f_{\max} = 1$ MHz. Our developed software running on a laptop computer can perform a complex 4096 point FFT within 2.4 ms and allows for fast online signal processing.

Another critical parameter is the excitation signal amplitude. Extremely low amplitudes in the mV or even sub-mV range cause difficulties associated with noise and the dynamic range of AD-converters. In contrast very high amplitudes in the range of several volts may significantly cause measurement errors due to the resulting high current densities and nonlinear behavior or even damage of the tissue under investigation. Based on our experience, we choose the chirp signal amplitude to be 100 mV as a compromise and use this value within all experiments.

V. Laboratory Measurement Setup

For experiments, a laboratory measurement setup is developed using state of the art equipment. Fig. 8 shows a block schematic of the implemented setup. The chirp signal is generated by a programmable arbitrary waveform generator (AWG, Tektronix AFG3252) which drives the coaxial cable connected to the needle via a current measurement resistor. The stimulating voltage signal and the resulting current signal are synchronously sampled by a digital storage oscilloscope (DSO, LeCroy WaveRunner 104 Xi). The AWG generates an additional trigger signal with stable phase relative to the chirp measurement signal and allows for a stable triggering and sampling. Both oscilloscope input channels have a limited input impedance of 1 MOhm and a relatively high input capacitance of approximately 20 pF. Especially at higher frequencies the high input capacitance causes a low input impedance and leads to frequency-dependent measurement errors. This unwanted effect is avoided by employing two identical buffer amplifiers connected to the oscilloscope inputs, as shown in Fig. 8. The amplifiers have an input capacitance of approximately 1 pF.

The software calculates the chirp signal and controls the signal generation and sampling process via LAN and USB. In addition, the software processes the measured raw data and directly calculates the transfer function. In principle the transfer function can directly be calculated out of the measured voltage and current signals, as illustrated in Fig. 7. Drawbacks of this direct method are measurement errors caused by inherent parasitic effects such as unwanted capacitive and resistive elements in the setup. Fig. 9 shows an equivalent circuit including major effects such as the cable capacitance C_c and the connector/cable resistance R_c. In order to minimize such measurement errors, we perform a one-time system calibration by measuring the transfer function of the "open" system (no load at the needle tip) and the "shortened" system (short circuit at the needle tip). The measured transfer functions of the open circuit and the shortened circuit are used to directly correct measurement errors of the tissue transfer functions in frequency domain. First, the "open" calibration has to be performed. In an ideal setup, no current is expected to flow under the "open" condition. In reality, a frequency-dependent current can be measured. This alternating current mainly flows through the parallel cable capacitance C_c. The equivalent schematic for an "open" condition is presented in Fig. 9(a).

The measured transfer function TF$\{$open$\}$ is directly the transfer function of the capacitive element TF$\{C_c\}$. Fig. 9(b) shows the equivalent circuit for a "short" condition on the needle tip. In parallel to the capacitance C_c there is two times the cable resistance R_c. The transfer function TF$\{R_c\}$ can be obtained by calculating TF$\{R_c\}$ = TF$\{$short$\}$ – TF$\{C_c\}$. Now all relevant parasitic components are known and the corresponding transfer functions can directly be taken into account during the calculation of any measured tissue transfer function. Fig. 10 shows two plots for a laboratory measurement result obtained by placing the needle tip into a resistive saline bath with a measured conductivity of 16.2 mS/cm (almost isotonic). In the test setup we used a coaxial cable of type RG174A with a length of 1.5 m to connect the needle with our measurement setup. In case of no calibration and no error correction, a signal degradation at high frequencies is observed. This is mainly caused by the parasitic coaxial cable capacitance. Applying the above described calibration procedure virtually eliminates the parasitic effects and shows a stable modulus and phase value as expected for a pure resistive load within this frequency range. Any polarization effects at low frequencies could not be observed within this experiment. According to [19] the polarization effect becomes more visible at frequencies below 1 kHz, which is outside of our measurement range.

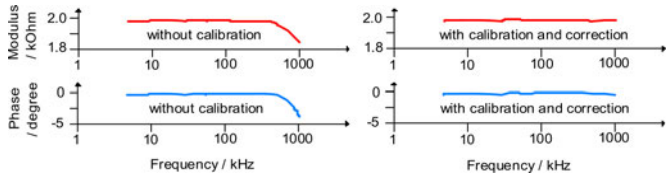

Fig. 10. Influence of parasitic components and result of calibration and error correction illustrated by the result of an experiment obtained in resistive saline bath.

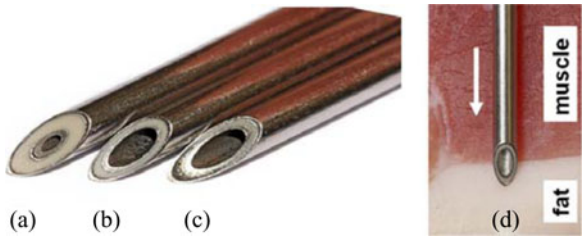

Fig. 11. Picture of three different hollow coaxial prototype needles. Needle C is used throughout the experiments, the dimensions are given in Fig. 1. Needles A and B are used during additional *in vitro* experiments. Picture 11D illustrates the setup used for *in vitro* experiments using well prepared tissue with good visible and sharp tissue boundaries between muscle and fat.

VI. Materials and Methods

A. Overview

Within this research study, we conducted several *in vivo* and *in vitro* experiments. Goal of the *in vivo* experiments was to derive measurement data especially in order to investigate the possibility of tissue classification. Details of the *in vivo* experiments are presented in Section VI-B in this paper. In addition to the *in vivo* experiments we conducted three *in vitro* experiments in order to investigate side effects and robustness of the measurement principle as well as verifying the FEM-simulation results presented in Section III. Details about the *in vitro* experiments are given in Section VI-C.

All measurements have been done with the developed laboratory setup described in Section V. The measurement resistor R (see Fig. 8) is set to 100 Ohm. The excited chirp signal had a duration of 200 μs, an amplitude of 100 mV, and covered a bandwidth from 5 kHz to 1 MHz. The signals have been captured by a DSO with a sampling rate of 20.48 MHz and an amplitude resolution of 8 bits resulting in a total number of 4096 samples per sampled chirp signal. The sampled waveforms of the stimulus chirp signal and resulting current signal have been stored on file for later analysis.

B. In vivo Experiments

All *in vivo* experiments have been conducted on anesthetized pigs. For our study, we measured on three pigs. On each pig the three-tissue types muscle, fat, and blood have been measured on two locations with a prototype needle having the dimensions presented in Fig. 1. A picture of the used prototype needle is shown in Fig. 11(c). First measurement location was the neck of the pig, and second measurement location was the hip of the pig. A veterinarian carefully cut the skin of the pig and dissected the named three-tissue samples. The samples were prepared in such a way that the measurement needle could be inserted into either plain muscle, fat, or arterial blood tissue without any visible inhomogeneity. Placement of the needles was done manually.

The *in vivo* experiments have been done in accordance with animal ethic standards approved by the government of Baden-Württemberg, Germany. Institutional and national guides for the care and use of laboratory animals were followed.

C. In vitro Experiments

Goal of the first *in vitro* experiment was to verify the simulation result for the expected spatial resolution of the tissue classification on the needle tip. Therefore, we inserted the needle into well prepared tissue [see Fig. 11(d)] using a programmable linear actuator. We started with the needle tip embedded inside homogeneous muscle tissue. In steps of 0.1 mm we moved the needle toward the fat tissue. On each step we measured the impedance spectrum of the tissue load. We stopped the actuator when the needle tip was fully embedded inside fat tissue.

The second *in vitro* experiment was conducted with the same setup, but the needle was moved within homogeneous muscle tissue only. We continuously moved the needle with various speeds from 0 to 14 $\mathrm{mm^{*}s^{-1}}$ and continuously measured during the movement. Goal was to evaluate if a moving needle shows different results compared to a non-moving needle due to disturbance effects of the double layer on the electrodes.

The third *in vitro* experiment was done with three different types of prototype needles with various dimensions, as shown in Fig. 11(a) and (b). All three needles were placed into homogeneous muscle and fat tissue and the impedance spectra have been recorded. The results are compared to each other and give a first overview about the impact of mechanical parameters on the tissue classification.

VII. Measurement Results

A. In vivo Experiments

During the *in vivo* experiments the three different tissue types muscle, fat, and arterial blood have been measured. The sampled raw data of the stimulus voltage signal and the response current signal have been processed by a custom analysis software according to the scheme presented in Fig. 7. The output of the signal processing software is a Bode diagram for each measurement. Since the measured impedance is complex there are two plots for each measurement—the modulus plot and the phase plot as a function of frequency. Below are the obtained results for the three tissues. We conducted the measurement on three pigs with two samples per pig resulting in a total of six measurements per tissue. However, for muscle tissue we only show five measurements since we had to exclude one extreme outlier. The outlier was caused by accidentally scratching a blood vessel and almost reflected the blood curve only.

B. In vitro Experiments

The first *in vitro* experiment was done in order to verify the simulation result presented in Fig. 4. The experiment was

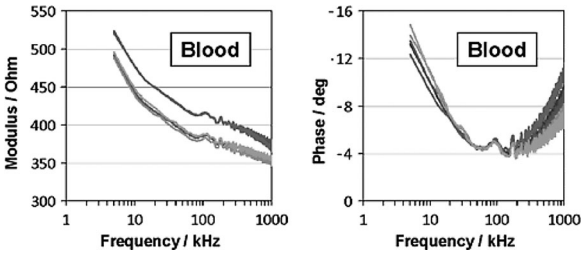

Fig. 12. Bode diagrams for blood measured using a 200 μs chirp signal. The left diagram shows the modulus and the right diagram shows the phase.

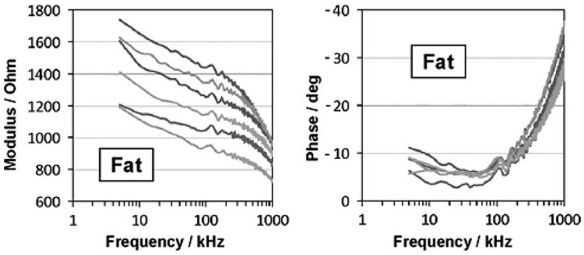

Fig. 13. Bode diagrams for fat measured using a 200 μs chirp signal. The left diagram shows the modulus and the right diagram shows the phase.

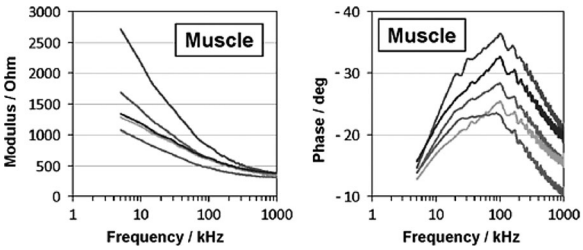

Fig. 14. Bode diagrams for muscle measured using a 200 μs chirp signal. The left diagram shows the modulus and the right diagram shows the phase.

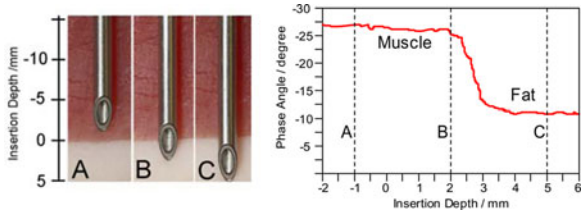

Fig. 15. *In vitro* experiment for evaluating the spatial measurement resolution. Three remarkable needle positions are shown in A, B, and C. The corresponding positions are also marked with A, B, and C in the phase diagram on the right side. The plotted phase curve shows the phase angle at a frequency of 100 kHz.

conducted as described in Section VI-C. Measurements were obtained for the needle transition from muscle to fat tissue. Fig. 15(a)–(c) illustrates the needle position as also indicated in the associated graph on the right side. The graph shows the measured phase as a function of the penetration depth for a fixed frequency of 100 kHz. We chose 100 kHz because according to Figs. 13 and 14, at this frequency we expect a significant change in the signal depending on which tissue we have in front of the needle tip.

The second *in vitro* experiment was done in order to verify the impact of speed when the needle is moving inside the tissue during the measurement cycle. The following graph shows the measured amplitude and phase values at a frequency of 100 kHz for muscle and fat tissue as a function of speed. The maximum speed which could be achieved with the given linear actuator was 14 $\mathrm{mm^{*}s^{-1}}$ which already represents a quite fast insertion process. During conventional surgical operations the needle insertion speed is usually lower.

The results obtained in the third *in vitro* experiment are presented later within Section IX because the data evaluation is also based on the tissue classification scheme discussed in Section IX. There the effect of the needle shape is discussed.

VIII. Discussion of Measurement Results

A. In vivo Experiments

The presented diagrams in Figs. 12–14 show the measured complex impedance formed by the tissues on the needle tip. The data include characteristic tissue properties as well as characteristic electrode polarization effects which cannot be separated from each other. However, on the first view, the three tissues seem to have individual characteristic shapes of the plotted curves. Especially the phase curves show significant differences in the shape and it looks attractive to classify the different tissue types based on their individual spectra. The classification approach is done using correlation and is described in detail within Section IX.

It is remarkable that all measured curves for blood show an almost perfect match to each other whereas especially the impedance curves for fat and the phase curves for muscle show some variations between the lines. According to our measurement experience this is mainly caused by the "quality" of the contact between the tissue and the needle. Blood is liquid and always has an ideal contact to the needle tip whereas the contact of fat and muscle tissue depends on the pressure which is generated by the needle. A high pressure ensures a good contact whereas a low pressure may significantly affect the measured values. However, the pressure is given by the mechanical tissue properties, the needle geometry, and the insertion speed. In real applications, this may vary and cannot be optimized or stabilized. For tissue classification, this circumstance should be included in the tests and a resulting classification scheme should be robust enough to correctly identify the different tissues despite the unknown "quality" of the contact to the needle. In addition to the variations caused by imperfections of the contact, there is the possibility that small inhomogeneities in the tested tissues caused variations as well.

B. In vitro Experiments

The measurement results for the first *in vitro* experiment are presented in Fig. 15. The graph shows the measured phase angle as a function of the insertion depth at a frequency of 100 kHz. The measurement values were picked out of the measured impedance spectrum, which has been recorded for each measurement position, as described in Section VI-C. The graph clearly shows that the measured phase value for muscle remains stable until the boundary layer of muscle and fat is reached with

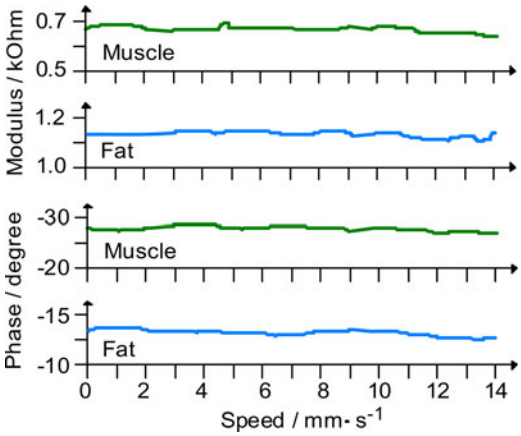

Fig. 16. Modulus and phase angle of the impedance as a function of needle insertion speed for muscle and fat tissue. The diagram represents the values for 100 kHz obtained from the measured impedance spectra.

the center of the needle tip, indicated with position B. Shortly after reaching position B, the signal drops to the value measured for fat where it remains stable again. It is remarkable that there is a "spatial delay" between position B and the falling signal edge, which is approximately 0.5 to 1.0 mm. This is caused by the higher electrical conductivity of the muscle tissue compared to the fat tissue (according to Fig. 16 approximately by a factor of two). As long as the needle tip still has contact to the muscle tissue with higher conductivity, the fat tissue is partially "shortened." This limits the steepness of the falling edge as well. However, according to the simulation result presented in Section III, the sensitivity of the system should be within 1 mm of the needle tip. The obtained measurement results support the simulation results very well. The falling signal edge occurs within 1 mm and the location of the falling edge is within 1 mm to the position B. In summary, the FEM simulation and the experimental results lead to the conclusion that the sensitivity is approximately within 1 mm to the needle tip for a needle with an outer diameter of 2 mm and therefore yields a very good spatial resolution which is ideal for precision needle tip placement inside a specific target tissue.

The second *in vitro* experiment shows the amplitude and phase values for muscle and fat tissue at 100 kHz as a function of speed of the moving needle. The results are presented in Fig. 16. The speed was varied from 0 to 14 $\mathrm{mm^{*}s^{-1}}$. Obviously, the measured values remain quite stable, which indicates that moving the needle within the tested speed regions and within the tested tissues does not significantly affect the measurements.

IX. Tissue Classification

A. Classification Method

Goal of the studies is to implement an online tissue classification system which enables to identify the type of tissue on the needle tip in real-time during the insertion process. Key component of such a system is a method that allows for identification of a specific tissue based on the characteristic properties of its spectrum. We use traditional correlation technique for "comparing" the shape of a measured spectrum with the shape of several known tissues contained in a "tissue transfer function library." Within our research, we obtained the "library functions" for each tissue by simply averaging the measured curves presented in Figs. 12–14. The averaged result for each tissue is presented below in Fig. 17.

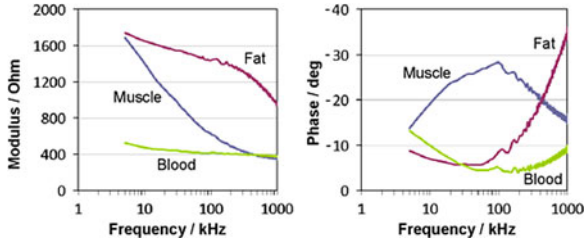

Fig. 17. Averaged curves from $n = 5$ measured transfer functions for muscle and $n = 6$ measured transfer functions for fat and blood tissue. All tissue types show an individual characteristic shape.

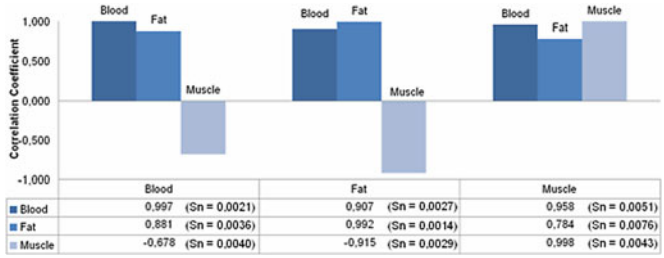

Fig. 18. The table shows the average correlation coefficients for the impedance modulus curves for each type of tissue correlated to each other averaged transfer function. The standard deviation is enclosed in brackets.

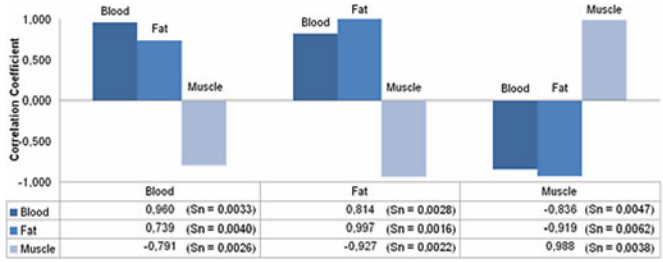

Fig. 19. The table shows the average correlation coefficients for the phase curves for each type of tissue correlated to each other averaged transfer function. The standard deviation is enclosed in brackets.

The obtained measurement data (modulus and phase diagrams) for each single measurement within each type of tissue are correlated to all three library functions presented in Fig. 17. The resulting correlation coefficients for impedance are presented in Fig. 18, the results for phase in Fig. 19. The tables show the obtained average value and the standard deviation enclosed in brackets. A correlation factor of 1 means both correlated curves are identical and, therefore, indicate a perfect match between the measured transfer function and the library transfer function. A coefficient of 0 shows that there are no similar properties and a coefficient of -1 indicates a perfect match associated with a negative relationship to the original curve.

In order to derive a robust tissue classification scheme, it is desirable to obtain a correlation coefficient close to 1 for the

matching curves (e.g., measured blood curve correlated with library blood curve) and a coefficient as close to zero as possible for non-matching curves (e.g., measured blood curve correlated with library muscle curve). Second important factor for a robust classification scheme is a tight standard deviation of all correlated values. This ensures proper classification even in the case that two average correlation factors for different tissues are relatively close to each other (e.g., blood to library blood = 0.9 and blood to library muscle = 0.8).

The data presented in Figs. 18 and 19 show that a tissue classification of the three tested tissues can be done without any trouble based on the experimental dataset. Classification can either be done on modulus or phase curves only whereas the phase curves show slightly better correlation results for classification. The standard deviation is at least by a factor of approximately 30 smaller than the smallest absolute difference in correlation coefficients (e.g., fat impedance correlated with library fat versus fat impedance curve correlated with library blood yields an average difference in the correlation coefficient of 0.992 – 0.907 = 0.085 whereas the standard deviation is 0.0027 for fat).

Another interesting point that has to be investigated is the effect of mechanical variations. Any variation in the needle geometry, variation in size, and mechanical tolerances as well as imperfections of the metal surface have impact on the effective electrode surface and thus affect the electrode transfer impedance to the tissue as well as the resulting current density inside the tissue. Since it is difficult to quantitatively cover the impact of all possible tolerances and variations, we simply manufactured two more needles with the same outer diameter of 2 mm but different inner conducting tubes and different PTFE insulation thicknesses. The two additional needles are shown in Fig. 11(a) and (b). Needle A has an inner diameter of 0.4 mm and 0.4 mm PTFE insulation, needle B has an inner diameter of 0.8 mm and 0.2 mm PTFE insulation. All three needles are used within the same *in vitro* experiment and it is measured ten times inside muscle and fat tissue with each needle. The derived transfer functions of all three needles have been correlated to "library functions" obtained by only averaging the values from the original needle C. That means we compare the measurement results from needles A and B to needle C using the correlation technique despite the needles have significantly different dimensions. The resulting correlation coefficients are presented in Table I. Tissue classification is still possible, but the average coefficients become closer to each other compared to the values shown in Figs. 18 and 19. That means less "buffer" for a definite tissue classification. However, it shows that the correlation method has good potential to be robust enough against mechanical imperfections caused by manufacturing of a needle with a well defined geometry.

TABLE I
CORRELATION COEFFICIENTS FOR NEEDLES A AND B

Needle C library functions	Modulus		Phase Angle	
	Needle A		Needle A	
	Muscle	Fat	Muscle	Fat
Muscle	0,932	-0,883	0,953	-0,901
Fat	0,661	0,928	-0,898	0,966
	Needle B		Needle B	
	Muscle	Fat	Muscle	Fat
Muscle	0,944	-0,957	0,979	-0,934
Fat	0,707	0,948	-0,933	0,972

B. Limitations

So far we only investigated the potential for classifying between homogeneous tissue types. Measuring a mix of tissue on the needle tip will cause the correlation method to fail as it is implemented right now. In further research, the classification algorithm has to be optimized. By combining modulus and phase data within the classification, there might be a way for a robust classification even for mixed tissue volumes containing at least two unknown tissue types. The system has to be further tested with more different tissue types as well as with human tissues.

X. CONCLUSION

Throughout this paper, we presented a novel system approach for online broadband impedance measurement and online tissue classification on the tip of a hollow needle. The developed system architecture shows good potential for building up a stand-alone needle guidance system or it could be integrated into existing needle steering systems. Here it can potentially improve the weakness of such systems that they often cannot perfectly classify between different types of soft tissue. The presented system architecture successfully uses short broadband chirp signals with well chosen parameters and a following effective signal processing scheme for obtaining transfer functions of the load on the needle tip within a very short measurement time as required by an online system. Tissue classification is done by simple correlation of the measured complex transfer functions. The measured functions are compared to known library functions and based on the correlation coefficients the type of tissue is identified. The *in vivo* experiments show excellent results and allow for a clear tissue identification using either the modulus or the phase curve of the transfer function whereas the results obtained by analyzing the phase curve are slightly better. Additional *in vitro* experiments indicate that the system has good potential to be robust against mechanical tolerances of the needle tip electrodes as well as to be almost immune against dynamic needle movement within the tested speed range up to $14\,\mathrm{mm^{*}s^{-1}}$. An FEM simulation and a corresponding *in vitro* experiment show an excellent spatial resolution of the sensitive needle tip, approximately 90% of the signal is derived within 1 mm to the needle tip for a needle with an outer diameter of 2 mm. This is a better resolution than existing prototype systems based on monopolar electrodes can achieve. According to [14], a spherical shaped monopolar electrode tip measures 70% of the total signal within a relatively large volume having a 3.3 times greater diameter than the needle. Clear advantage of the proposed coaxial needle design is in the close proximity of the two electrodes at the needle tip and the resulting well defined current path.

REFERENCES

[1] D. Popovic and M. Okoniewski, "Precision open-ended coaxial probe for dielectric spectroscopy of breast tissue," in *Proc. IEEE Antennas Propag. Soc. Int. Symp. 2002*, vol. 1, pp. 815–818.

[2] M. Vosseler, M. Jugl, and R. Zengerle, "A smart interface for reliable intradermal injection and infusion of high and low viscosity solutions," *Pharm. Res.*, vol. 28, pp. 647–661, 2011.

[3] Y. Thakur, J. S. Bax, D. W. Holdsworth, and M. Drangova, "Design and performance evaluation of a remote catheter navigation system," *IEEE Trans. Biomed. Eng.*, vol. 56, no. 7, pp. 1901–1908, Jul. 2009.

[4] H. Saito and T. Togawa, "Detection of puncturing vessel wall for automatic blood sampling," in *Proc. 1st Joint BMES/EMBS Conf., 1999*, vol. 2, Atlanta, GA, Oct.1999, p. 866.

[5] R. Alterovitz, J. Pouliot, R. Taschereau, I. Hsu, and K. Goldberg, "Simulating needle insertion and radioactive seed implantation for prostate brachytherapy," *Stud. Health Tech. Informat.*, vol. 94, pp. 19–25, 2003.

[6] R. Viard, N. Betrouni, J. Rousseau, S. Mordon, O. Ernst, and S. Maouche, "Needle positioning in interventional MRI procedure: Real time optical localisation and accordance with the roadmap," in *Proc. 29th Annu.IEEE Int. Conf. Eng. Med. Biol. Soc. (EMBS) 2007*, Lyon, France, Aug. 22–26,, pp. 2748–2751.

[7] G. Fichtinger, A. Deguet, K. Masamune, E. Balogh, G. S. Fischer, H. Mathieu, R. H. Taylor, S. J. Zinreich, and L. M. Fayad, "Image overlay guidance for needle insertion in CT scanner," *IEEE Trans. Biomed. Eng.*, vol. 52, no. 8, pp. 1415–1424, Aug. 2005.

[8] B. Bascle, N. Navab, M. Loser, B. Geiger, and R. Taylor, "Needle placement under X-ray fluoroscopy using perspective invariants," in *Proc.. IEEE Workshop Math. Methods Biomed. Image Anal., 2000*, Hilton Head Island, SC, Jun. 11–12,, pp. 46–53.

[9] R. S. Singh, S. Natarajan, M. Lee, A. E. Dann, B. P. Cox, D. B. Bennett, E. R. Brown, H. Lee, W. S. Grundfest, and M. O. Culjat, "Development of an ultrasound imaging system for needle guidance," in *Proc. IEEE Int. Ultrason. Symp. (IUS) 2009*, Rome, Sep. 20–23,, pp. 1852–1855.

[10] S. Cochran, G. A. Corner, K. J. Kirk, D. I. A. Lines, and M. J. Watson, "P5 C-5 design and validation of an ultrasound array optimised for epidural needle guidance," in *Proc. IEEE Ultrason. Symp., 2007*, Oct. 28–31, pp. 2255–2258.

[11] A. Haddadi, O. Goksel, S. E. Salcudean, and K. Hashtrudi-Zaad, "On the controllability of dynamic model-based needle insertion in soft tissue," in *Proc. 2010 IEEE Annu. Int. Conf. Eng. Med. Biol. Soc. (EMBC)*, Buenos Aires, Argentina, Aug. 31–Sep. 4, pp. 2287–2291.

[12] A. Majewicz, T. R. Wedlick, K. B. Reed, and A. M. Okamura, "Evaluation of robotic needle steering in ex vivo tissue," in *Proc. 2010 IEEE Int. Conf. Robot. Autom. (ICRA)*, Anchorage, AK, May 3–7, pp. 2068–2073.

[13] W. Yang, A. Bonvilain, T. Alonso, A. Moreau-Gaudry, and S. Basrour, "Modeling and characterization of an instrumented medical needle in sight of new microsensor design for its insertion guidance," in *Proc. 2010 IEEE Annu. Int. Conf. Eng. Med. Biol. Soc. (EMBC)*, Buenos Aires, Argentina, Aug. 31–Sep. 4, pp. 6465–6468.

[14] H. Kalvoy, O. G. Martinsen, and S. Grimnes, "Determination of tissue type surrounding a needle tip by electrical bioimpedance," in *Proc. 30th IEEE Annu. Int. Conf. Eng. Med. Biol. Soc. (EMBS) 2008*, Vancouver, BC, Aug. 20–25,, pp. 2285–2286.

[15] H. Kalvoy, L. Frich, S. Grimnes, G. Martinsen, P. K. Hol, and A. Stubbhaug, "Impedance based tissue discrimination for needle guidance," *Physiol. Meas.*, vol. 30, pp. 129–140, 2009.

[16] D. Trebbels, M. Jugl, and R. Zengerle, "Real-time cannula navigation in biological tissue with high temporal and spatial resolution based on impedance spectroscopy," in *Proc. Annu. IEEE Int. Conf. Eng. Med. Biol. Soc. (EMBC) 2010*, Buenos Aires, Argentina, Aug. 31–Sep. 4, pp. 1886–1889.

[17] S. Gabriel, R. W. Lau, and C. Gabriel, "The dielectric properties of biological tissues: II. Measurements in the frequency range 10 Hz to 20 GHz," *Phys. Med. Biol.*, vol. 41, pp. 2251–2269, 1996.

[18] S. Grimnes and O. G. Martinsen, *Bioimpedance and Bioelectricity Basics*. Oxford, UK: Academic Press, 2000.

[19] U. Pliquett, D. Frense, M. Schönfeldt, C. Fratzer, Y. Zhang, B. Cahill, M. Metzen, A. Barthel, T. Nacke, and D. Beckmann, "Testing miniaturized electrodes for impedance measurements within the beta-dispersion—A practical approach," *J. Electr. Bioimpedance*, vol. 1, pp. 41–55, 2010.

[20] T. Paavle, M. Min, and T. Parve, "Using of chirp excitation for bioimpedance estimation: Theoretical aspects and modeling," in *Proc. 11th Int. Biennial Baltic Electron. Conf. (BEC) 2008*, Tallinn, Estonia, Oct. 6–8, pp. 325–328.

Authors' photographs and biographies not available at the time of publication.